Microstructure, mechanical properties and tribo-corrosion mechanism of $(CrNbTiAlVMo)_xN_{1-x}$ coated 316 L stainless steel in 3.5 wt% NaCl solution

Dewen Niu [a,c], Cunxiu Zhang [a,c], Xudong Sui [a,b,d,*], Xiaolong Lu [a,b,d], Xiao Zhang [a,b,d], Cong Wang [a,b], Junying Hao [a,b,d,*], Zhiqiang Shi [c]

[a] State Key Laboratory of Solid Lubrication, Lanzhou Institute of Chemical Physics, Chinese Academy of Science, Lanzhou 730000, China
[b] Center of Materials Science and Optoelectronics Engineering, University of Chinese Academy of Sciences, Beijing 100049, China
[c] Department of Materials Science and Engineering, China University of Petroleum (East China), Qingdao 266580, China
[d] Qingdao Center of Resource Chemistry and New Materials, Qingdao 266000, China

ABSTRACT

$(CrNbTiAlVMo)_xN_{1-x}$ coatings were deposited on 316 L steel by sputtering method. The structure, mechanical and tribo-corrosion performances of the coating were studied. The results show that all coatings exhibit single FCC structure. With the increase of Mo content, the surface particle size increases, and the orientation changes from (111) to (200). The maximum hardness reaches 44.3 GPa and the corresponding elastic modulus is 405 GPa. Tribo-corrosion test show that the coatings exhibit better resistance to tribo-corrosion than 316 L steel. The coating with 8 at% Mo content has the lowest static current density (7.49×10^{-9} A/cm^2) and dynamic current density (9.33×10^{-8} A/cm^2), while the coating with 32 at% Mo content shows the smallest wear volume. The related synergistic mechanism of tribo-corrosion was discussed.

1. Introduction

With the development of the marine industry, many engineering components (such as valves, pumps, lifting systems, etc.) suffer from the adverse effects of corrosion, which is manifested as a large number of component failures and huge economic losses [1]. 316 L stainless steel has been widely used because of its excellent corrosion resistance in various environments [2–7]. Higher Cr content in 316 L is beneficial to promote the formation of surface passivation film, which further improves its corrosion resistance. However, the combination of the removal of the film and the corrosive environment leads to accelerated corrosion [8]. Therefore, there are many problems to be solved for 316 L stainless steel used in tribo-corrosion environment.

In recent years, high-entropy alloys (HEAs) have been widely studied as a material with good corrosion resistance and wear resistance [9–15]. Compared with conventional materials, HEAs have better fracture resistance [16], hardness [17,18], oxidation resistance [19] and corrosion resistance, which is attributed to four core effects, including high-entropy effect, slow diffusion effect, lattice distortion effect and cocktail effect [19–21] However, the processing cost limits the wide

application of HEAs. Recently, the concept of high-entropy alloy coatings (HEACs) have been proposed. Benefiting from the lower dimension of the coating material, the HEACs not only have similar properties to the high-entropy alloy bulk, but also exhibit superior strength and toughness. In general, HEACs exhibit mostly simple single or amorphous structure. At the same time, the elemental composition of HEACs is more complex, which can easily regulate the corrosion resistance [22,23]. For instance, Dou et al. [24] found that FeAlCoCuNiY HEAC had a single FCC structure without component segregation. And the coating had better corrosion resistance than 201 stainless steel. It was found that Fe, Co, and Ni increase the passivation area and corrosion resistance of AlCoFeNiTiZr HEAC [25]. At the same time, the grain refinement also makes the HEAC have better corrosion resistance. Bachni et al. [26] researched the effect of Al content on corrosion performance of VNbMoTaWAl. They found that the corrosion resistance of coating was the best when Al content in the coating was 2.37 at%.

Recently, nitrogen is introduced into HEACs to form high-entropy ceramics or high-entropy nitride coatings (HENCs). The addition of N element plays a role in solid solution strengthening, which exhibits better mechanical properties. So far, many studies on HENCs have been

reported [27–33]. Most of them focus on the structure, mechanical properties, friction properties and corrosion. Zhang et al.[34] reported that the microstructure become dense and the friction changes significantly of (TiVCrNbSiTaBY)N HENCs with the increase of bias voltage. (AlCrMoSiTi)N$_x$ coating was reported that the crystal structure gradually changed to FCC structure with the increase of nitrogen content [35]. And when the nitrogen content was 49 at%, high hardness (41.6 GPA) coating showed excellent mechanical. Lo et al. demonstrated that the (AlCrNbSiTiMo)N coating deposited at − 100 V had lowest wear rate of 1.2×10^{-6} mm^3/Nm at 700 ℃. [36]. Si et al. [37] discovered that the corrosion resistance of TiVCrZrWN$_x$ coatings increased with the increment of N content. But few papers focus on synergistic effect of wear and corrosion on coatings.

In this paper, six strong nitrogen compound elements (Cr, Nb, Ti, Al, V, Mo) were selected to deposit coatings. According to previous studies, the selected Cr, Ti, Al and Mo elements are proved to easily form a passivation film in 3.5 wt% NaCl solution and enhance the corrosion resistance of the coatings [38–40]. The oxides formed by selected Mo, V and Nb elements during the friction process are beneficial to reducing friction [41,42]. Many studies have found that Mo doping has a significant effect on the hardness, friction coefficient and corrosion resistance of the coating [43,44]. However, to the best of our knowledge, most of the articles study the friction or corrosion behavior independently, and there are fewer studies focus on the synergistic mechanism of wear and corrosion. Therefore, a series of (CrNbTiAlVMo)$_x$N$_{1-x}$ coatings with different Mo content were prepared in this paper. The mechanical properties, microstructure and tribo-corrosion mechanism of as-deposited coatings were systematically investigated in relation to the Mo content.

2. Experimental details

2.1. Deposition of (CrNbTiAlVMo)$_x$N$_{1-x}$ coatings

(CrNbTiAlVMo)$_x$N$_{1-x}$ coatings with different Mo contents were deposited on Si wafers and 316 L substrates using an unbalanced magnetron sputtering system as shown in Fig. 1. The Si wafer was used to observe the cross-sectional morphology of the as-deposited coatings. The 316 L substrate was used to characterize the mechanical properties and to perform tribological tests of the coatings. Before the coating deposition, the bulks were ultrasonically cleaned four times with petroleum ether and alcohol in turn. They were fixed on the stand and rotated at a constant speed of 5 rpm. When the chamber pressure was

Fig. 1. Unbalanced magnetron sputtering system.

lower than 3×10^{-5} Torr, the surface of the substrate was first cleaned by sputtering with Ar$^+$ bombardment for 30 min to remove contaminants. The deposition process of the (CrNbTiAlVMo)$_x$N$_{1-x}$ coating was divided into two steps. In the first step, the Cr interlayer was deposited using a pure Cr target (99.9 at%) as a sputtering resource. The sputtering current and time were 4 A and 8 min, respectively. Second, the current of the Mo target and Cr-Nb-Ti-Al-V splicing target gradually increased to 4.5 A in 6 min. The nitrogen was used as the reactive gas and adjusted to 38 sccm during coating deposition. The detailed process parameters are listed in Table 1. To facilitate the following discussion, the (CrNbTiAlVMo)$_x$N$_{1-x}$ coatings with different Mo target currents are named S1, S2 and S3, respectively.

2.2. Characterization of (CrNbTiAlVMo)$_x$N$_{1-x}$ coating

Using field emission scanning electron microscopy (FESEM, JSM, 7610 F) to observe coating thickness, surface and cross-sectional morphology. X-ray diffraction (XRD, Bruker D 8 Advance) was used for examine the crystal structure of coatings. The details of the XRD test were scanned over a range of $35° - 50°$ at a speed of 0.02 (°)/min. X-ray photoelectron spectroscopy (XPS, Thermo K-Alpha$^+$) with Al Kα X-ray source at a power of 150 W was used to characterize the chemical composition of the coatings. Nano Indenter (Agilent XP) measured the hardness and Young's modulus of the coatings in load-unload mode. The indentation depth was set to 100 nm for data accuracy. The indentation depth was set to 100 nm for data accuracy. Each sample was measured 5 times at different area to reduce the error.

2.3. Electrochemical and tribo-corrosion test of (CrNbTiAlVMo)$_x$N$_{1-x}$ coating

As shown in Fig. 2, the electrochemical and tribo-corrosion performances of the coatings in 3.5 wt% NaCl solution at room temperature were both tested by using a liner reciprocating tribo-corrosion device (MFT 4000, Lanzhou Huahui) with a three electrode system. Carbon worked as counter electrode (CE), Ag/AgCl worked as reference electrode (RE) and the prepared samples worked as working electrode (WE). The exposed area of WE and was 2.25 cm^2. In static corrosion test, the scanning potential range varied from − 0.6–0.6 V with the speed at 0.333 mV/s, and the scan time was guaranteed to be 1 h. Before the test, soaked the samples for at least 1 h to ensure the samples reached a stable electricity state. In the tribo-corrosion test, Al$_2$O$_3$ balls (Φ 6 mm) were used as the friction pair. The load applied in the tribo-corrosion test is 5 N, the sliding frequency was 0.1 Hz, and striking stroke was 5 mm. The tribo-corrosion test performed under the open circuit potential (OCP) condition included three sections, soaking for 10 min, sliding for 60 min, and removed the load then soaking for 10 min. For the tribo-corrosion test performed under potentiodynamic polarization (PDP) conditions, sweeping the potential range from − 0.6–0.6 V at a speed of 0.333 mV/s. Wear for one hour at a potential of − 0.6 V in a 3.5 wt% NaCl solution is considered a pure wear test. After the test, the 3D profile of the wear track was measured by 3D profiler (MicroXAM 800, America).

Table 1
Deposition parameters of (CrNbTiAlVMo)$_x$N$_{1-x}$ coating by magnetron sputtering system.

Deposition parameters	Values
Splicing target current (A)	4.5
Mo target current (A)	1, 2 and 3 for S1, S2, S3 respectively
Working pressure (Torr)	3.8×10^{-3}
Bias voltage (V)	-96
Ar flow (sccm)	18
N$_2$ flow (sccm)	38
Deposition time (min)	150

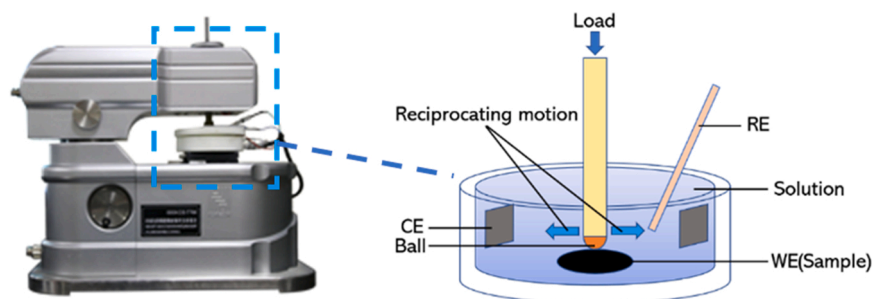**Fig. 2.** The structure of tribo-corrosion device.

3. Result and discussion

3.1. Microstructure and mechanical characterization of (CrNbTiAlVMo)$_x$N$_{1-x}$ coating

The surface and cross-sectional images of the coatings are shown in Fig. 3. The particles on the surface of the coatings are dome-shaped, and the cross-sectional morphologies are classical columnar structure. With the increase of Mo target current, the thickness of the coating increases from 800 to 1750 nm, and the corresponding surface particle size also increases. Generally, an increase in target current results in an increase in the deposition rate of the coating. The composition of the coating was determined by XPS, and the results are shown in Table 2. Obviously, with the increase of molybdenum target current, the molybdenum content in the coating also increases. The content of other elements fluctuates within a certain range. The S3 has the highest Mo content at 32%. At the same time, we can calculate the mixing entropy of each coating according to the following formula:

$$\Delta S_{mix} = -R \sum_{i=1}^{n} c_i ln c_i \tag{1}$$

Where c_i is the atomic ratio of the element and R is the gas constant (8.314 J mol^{-1} K^{-1}). The calculated ΔS_{mix} value of the as-deposited coating is listed in Table 2. As for the S3 coating, the ΔS_{mix} is 13.08 kj/mol ($\geq$1.5 R), which is consistent with the definition of HEAs

Table 2
Chemical compositions (at%) and ΔS_{mix}(kj/mol) of the samples.

Sample	Cr	V	Ti	N	Mo	Nb	Al	ΔS_{mix}
S1	11	3	3	57	8	4	14	11.51
S2	7	2	2	67	13	2	7	9.51
S3	11	3	4	36	32	4	10	13.08

proposed by Yeh et al.[20].

As shown in Fig. 4, there are three strong diffraction peaks at 36.2°, 42.3° and 44.5° appearing on the XRD spectrum of the S1 coating. These correspond to the (111) and (200) diffraction peaks of the FCC structure and the diffraction peak of the transition layer Cr (44.9°), respectively [45,46]. It can be clearly seen that there is no formation of intermetallic compound. (111) is the optimal densely packed plane with the lowest strain energy for FCC. This is conducive to the formation of (111) preferential orientation in competitive growth. The preferred orientation of (200) is the preferred minimum surface energy. Therefore, all the coatings show (111) and (200) preferred orientation [47]. With the increase of coating thickness, the FCC structure signal gradually increases, while the Cr signal gradually decreases. With the power of the Mo target gradually increases, the preferred orientation of the coating gradually changed from (111) to (200). This phenomenon can be linked to thermodynamic and kinetic aspects. From a thermodynamic point of view, the coating structure generally tend to have minimal strain and surface
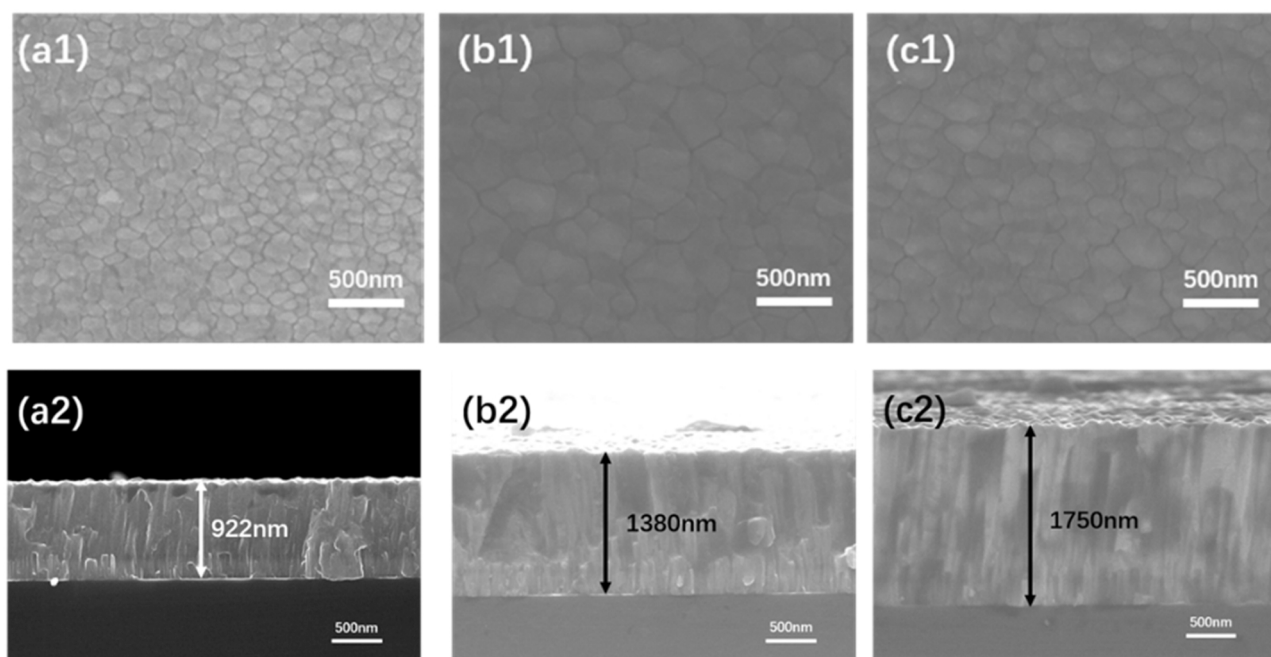

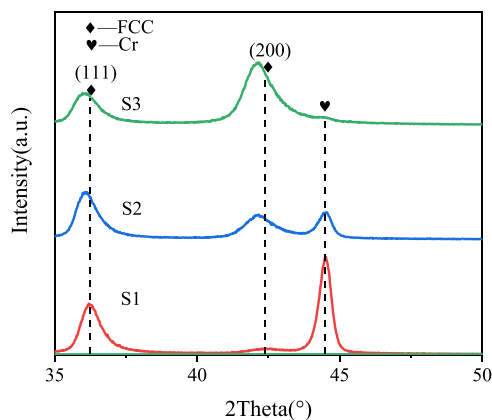**Fig. 3.** Surface and cross-sectional SEM images of (CrNbTiAlVMo)$_x$N$_{1-x}$. (a1, a2) S1; (b1, b2) S2; (c1, c2) S3.

Fig. 4. XRD patterns of (CrNbTiAlVMo)$_x$N$_{1-x}$ coating.

energy. The power of the Mo target increases gradually, the energy of the Mo atoms gradually increases and the mobility of the atoms increases. The atoms are easier to grow in (200) direction with low surface energy [48]. In terms of kinetic, the (200) direction is more likely to form channels for high-energy atoms [49]. Therefore, with the increase of Mo atoms, it gradually tends to grow in the (200) orientation.

Fig. 5(a) shows the evolution in hardness and modulus of (CrNbTiAlVMo)$_x$N$_{1-x}$ coatings. Clearly seen that the hardness and elastic modulus of the coatings decrease first and then increase with the increase of Mo content. S1 has the maximum hardness value of 44.3 GPa and elastic modulus value of 405 GPa. On the on hand, the coating with (111) preferred orientation exhibits higher hardness. As the Mo content changes, the preferred orientation of the coatings gradually changed from (111) to (200). Among them, the preferred orientation of S1 is (111). On the other hand, the intensity of the XRD peak indicates better crystalline properties. The (111) signal of S1 is the strongest. So S1 has the highest hardness. The value of H/E in Fig. 4(b) indicates its fracture resistance [50], while H^3/E^2 indicates its plastic deformation resistance [51]. It can be seen that the H/E and H^3/E^2 of S1 are the highest. The S1 coating has the best mechanical properties.

3.2. Tribo-corrosion performance of (CrNbTiAlVMo) $_{1-x}$ N$_x$ coating in 3.5 wt% NaCl solution

3.2.1. Tribo-corrosion performance under OCP condition

Fig. 6 shows the tribo-corrosion performance of 316Land coatings under OCP condition. Clearly seen that the OCP value of the as-deposited coatings are approximately − 0.05 V, which is higher than that of the substrate. The higher OCP value usually indicates better corrosion resistance. When the friction pair contacts the sample surface,
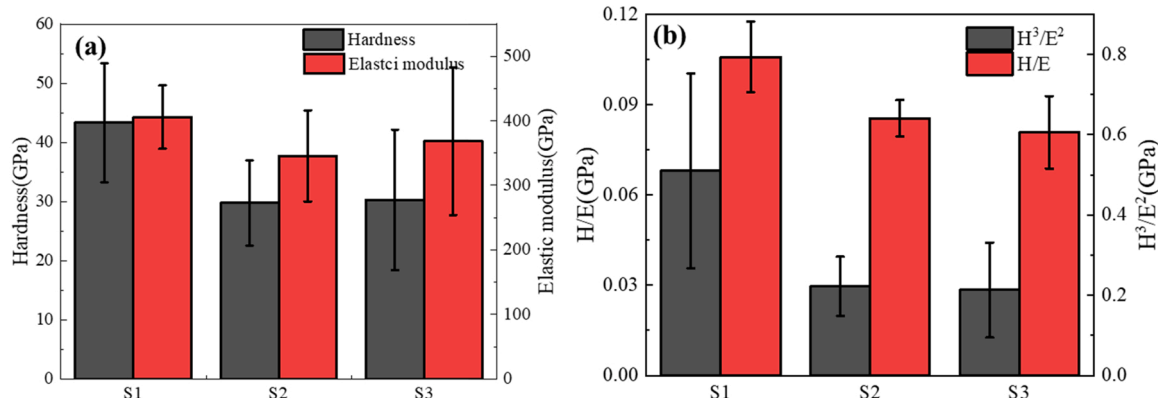
the measured potential changes. The potential of 316 L decrease to − 0.26 V, while potential of the coating decrease slightly. It can be seen in the layer that the potential gradually increased during the tribo-corrosion process from S1 to S3 with the increase of Mo content. S3 has the strongest resistance to potential change, which is related to the increase of Mo content [52]. This can be explained that the mechanical action of the friction pair removes the passivation film on the surface and exposing the fresh surface [53]. With the progress of wear, the potential gradually stabilizes and the formation and removal speed of the passivation film reaches a dynamic balance. After removing the load, the OCP of 316 L and coatings gradually increase as the passivation film recovered again on the samples [44]. In addition, it is worth noting that the coefficient of friction between the coating and 316 steel in NaCl solution is not much different, both around 0.15.

Fig. 7 is SEM images of the wear track after tribo-corrosion test. It can be found from Fig. 7**(a)** that the 316 L steel is severely worn, mainly manifested as abrasion. However, the wear tracks of as-deposited coatings are shallower and smoother than that of 316 L, which is mainly due to the high hardness of the coating. With the increase of Mo content, the wear mechanism of the coating gradually changes from abrasion to oxidation wear. This is mainly due to the good lubrication effect of oxides formed in the process of tribo-corrosion compared with the 316 L [54].

3.2.2. Tribo-corrosion performance under dynamic polarization condition

Fig. 8 shows the static polarization and PDP results of 316 L and the prepared coatings. The calculated self-corrosion potential (E$_{corr}$) and self-corrosion current density (I$_{corr}$) are shown in Table 3. Under the static polarization test, it can be seen that the S1 coating has the minimum I$_{corr}$ (7.04 ×10^{-8}A/cm^2) and higher E$_{corr}$ (−0.15 V). As the Mo content increases, the I$_{corr}$ of the coating increases, and the S3 coating gets the highest I$_{corr}$ (2.02 ×10^{-7} A/cm^2). Under the PDP test, the S1 coating still has the minimum I$_{corr}$ (9.33 ×10^{-8} A/cm^2), which is an order of magnitude lower than other samples. However, with the increase of Mo content, the E$_{corr}$ shows a gradually increasing trend. In general, the current density indicates the corrosion rate. In this paper, the dynamic current density is significantly higher than the static current density, which indicates that the friction behavior can promote the corrosion. The calculated wear volume measured by the 3D profilometer is shown in Fig. 8(c). The pure wear volume is obtained after friction by applied a cathodic protection potential of − 0.6 V in the 3.5 wt% NaCl solution. The wear volume of sliding under dynamic corrosion condition is calculated from Fig. 8(b). Compared to the 316 L steel, the wear volume of the coated samples under different conditions is much lower, which indicates the excellent tribo-corrosion performance of the prepared (CrNbTiAlVMo)$_x$N$_{1-x}$ coatings. Among them, the S3 coating owns the lowest wear volume under both condition.

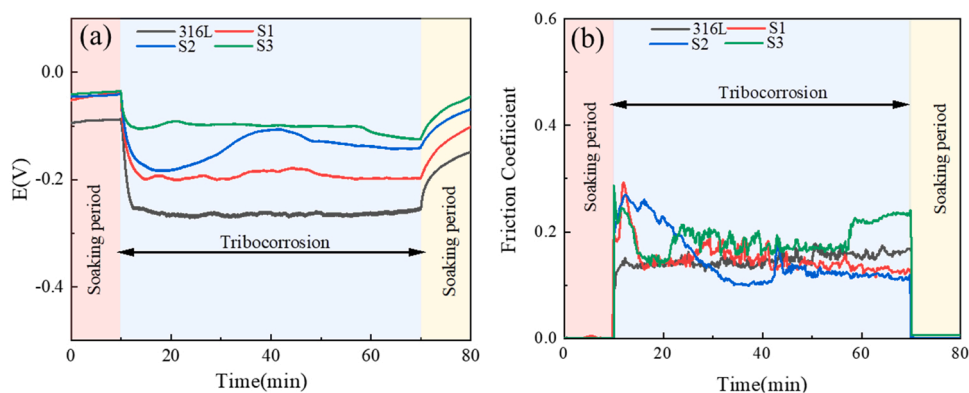Fig. 9 presents the wear track morphology of the coatings after PDP

Fig. 5. (a) Hardness and elastic modulus and (b) H/E and H^3/E^2.

Fig. 6. OCP measurements and respective friction coefficient curves of (CrNbTiAlVMo)$_x$N$_{1-x}$ coatings sliding against Al$_2$O$_3$ balls in 3.5 wt% NaCl solution.

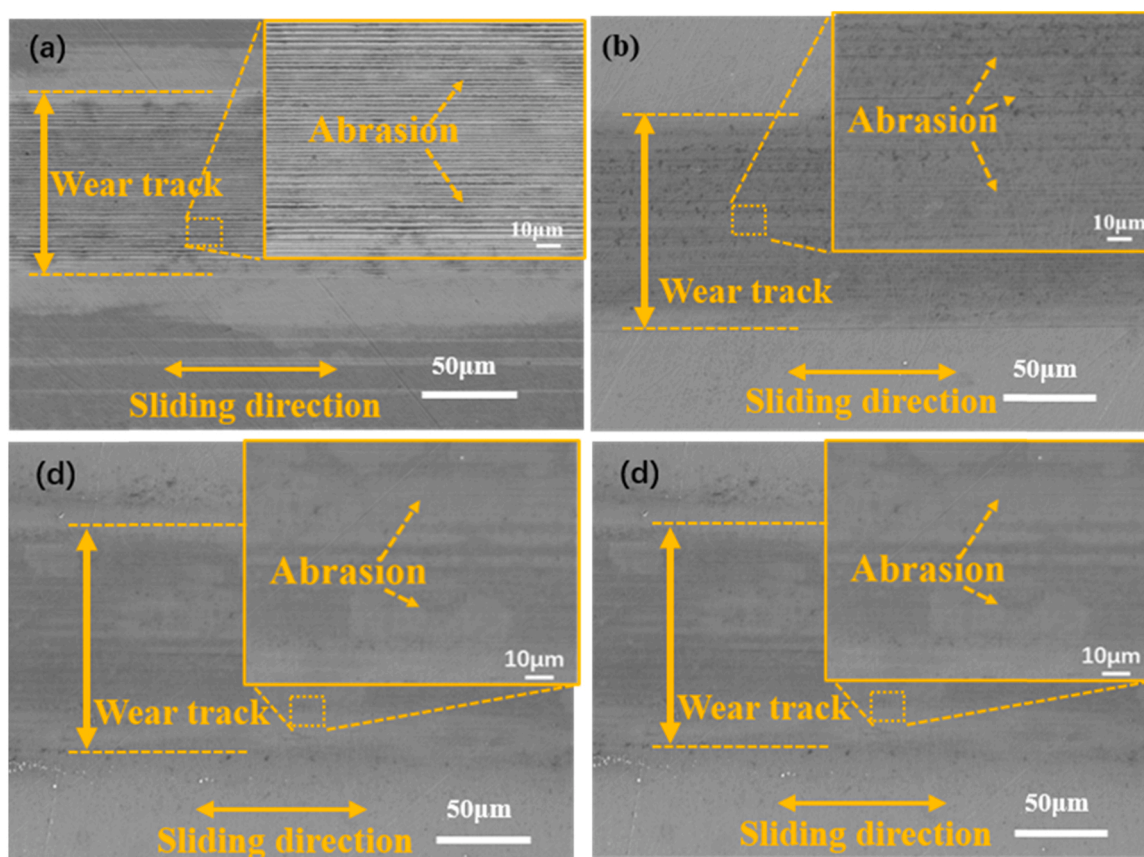**Fig. 7.** SEM images of wear tracks for 316 L alloy and (CrNbTiAlVMo)$_x$N$_{1-x}$ coatings under OCP condition. (a) 316 L; (b) S1; (c) S2and(d) S3.

test. The 316 L steel suffers severe pitting corrosion and abrasion, while no obvious pitting corrosion occurred in the coated samples. The wear track of S1 shown in Fig. 9(b) is shallow, and a bit corrosion pits appear on the wear track. The wear type of S1 is adhesive wear. It can be seen from Fig. 9(c) that there are a large number of particles on the wear track surface. It is clear that the wear type of S2 is particle wear. The low hardness causes the wear volume of S2 to be larger than that of S1 and S3. The wear track of S3 (Fig. 9(d)) is the smoothest, indicating that S3 has a better synergistic effect against wear and corrosion. In addition, XPS was used to determine the composition of wear tracks and the obtained results are shown in Table 4. The content of oxygen elements of wear tracks from S1 to S3 were 34.07, 31.87 and 16.89 at%, respectively. The reduced oxygen level in wear track may suggest less wear of the coating. Among them, the oxygen content of S1coating is the

highest, which indicates a large number of oxide film generated during the process of tribo-corrosion. This also explains the best corrosion resistance of the S1 coating.

3.3. Tribo-corrosion mechanism of (CrNbTiAlVMo)$_x$N$_{1-x}$ coatings

To study the tribo-corrosion mechanism of the coating, we assume that the volume losses only occur in the wear track under the process of tribo-corrosion test. This assumption was also adopted in some previous study[55,56]. Generally, the volume (T) lost in the process of tribo-corrosion can be divided into two parts: wear loss volume ($\triangle W$) and corrosion loss volume ($\triangle C$). The $\triangle W$ can be divided into two parts: pure wear loss volume (W) and wear increment volume (W_C): (1) the volume lost without corrosion is W, which is generally measured under
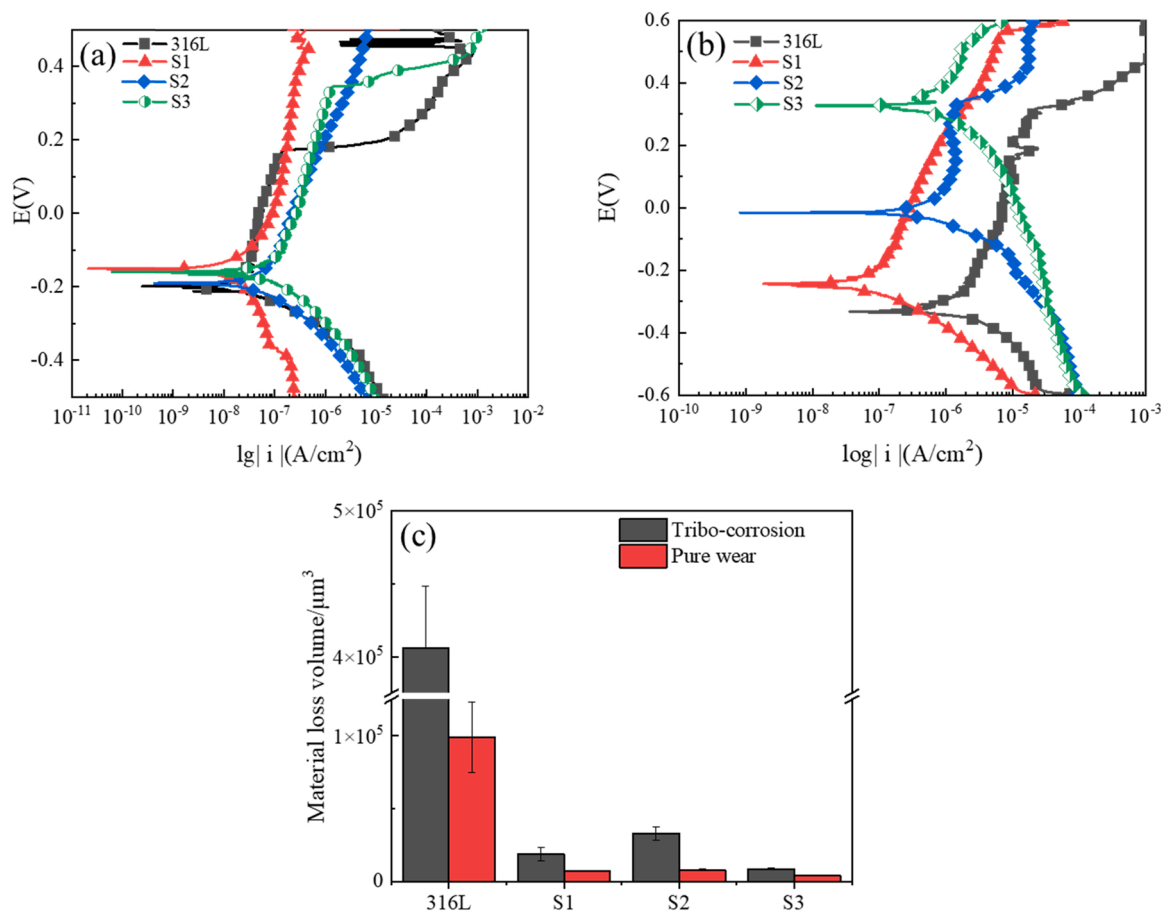
Fig. 8. Polarization curves under the condition of (a) pure corrosion and (b) tribo-corrosion; (c) wear loss volumes for 316 L and $(CrNbTiAlVMo)_xN_{1-x}$ coatings at pure wear test and tribo-corrosion test under PDP.

Table 3
Dynamic polarization results of $(CrNbTiAlVMo)_xN_{1-x}$ coatings in 3.5 wt% NaCl solution.

Condition	Sample	I_{corr} (A/cm^2)	E_{corr} (V)
Static Corrosion	316 L	3.55×10^{-8}	-0.20 V
	S1	7.04×10^{-9}	-0.15 V
	S2	6.29×10^{-8}	-0.19 V
	S3	2.02×10^{-7}	-0.16 V
Sliding Corrosion	316 L	3.07×10^{-7}	-0.33 V
	S1	9.33×10^{-8}	-0.24 V
	S2	2.51×10^{-7}	-0.01 V
	S3	2.44×10^{-7}	0.33 V

cathodic protection; (2) In the process of tribo-corrosion test, corrosion will cause the change of sample surface state, resulting in the change of wear loss volume. Compared with W the promoting effect of corrosion on wear is W_C. The $\triangle C$ is divided into pure corrosion loss volume (C_0) and corrosion increment volume (C_W): (1) the loss volume without wear is C_0. (2) Wear will destroy the passivation film on the sample surface, resulting in the change of corrosion loss volume. This part of the changed volume is produced by the promoting effect of wear on corrosion, which can be defined as C_W.

The wear loss volume is obtained under the condition of wear and corrosion. Each wear track is measured three times at different parts and then converted into the total volume to ensure the accuracy of the data. The volume of pure corrosion loss in the case of static corrosion and the total volume of corrosion loss in the process of tribo-corrosion are calculated by Faraday's law.

$$C_0 = \frac{itM}{nF\rho} \tag{2}$$

Where, i is the average current (A), the polarization curve obtained from the corrosion test by Tafel extrapolation, as shown in Table 2, and then multiplied by the exposed area. And t is the total test time (s), M is the molar mass of the coating (g / mol), n is the number of electrons transferred during the tribo-corrosion test, and F is the Faraday constant (C / mol). And ρ is the density of the coating (g / cm^3). Then the total volume lost (T) is:

$$T = W + C_0 + W_C + C_W \tag{3}$$

Fig. 10 shows the proportion of each component in the tribo-corrosion process of 316 L, S1, S2 and S3. It can be seen that the material loss volume of 316 L stainless steel is the largest, which mainly due to friction increment (W_C, 72.65%) and corrosion increment (C_W, 23.51%). The result shows that 316 L stainless steel has weak resistance to tribo-corrosion, especially the increase of corrosion on friction loss volume. It shows that corrosion damages the surface greatly, resulting in an increase in surface defects and a large change in the amount of wear. Among the prepared coatings, the loss volume of S3 is the smallest and the proportion of each loss is relatively uniform, indicating the high Mo content the coating has better tribo-corrosion resistance. The wear volume of S2 is the largest. Since the coating surface is the roughest in the process of wear and corrosion, the wear amount of S2 accounts for a large proportion. The total loss volume of S1 is smaller than S2, and the dominant wear volume can be explained by lower tribo-corrosion synergistic effect. In all coatings, ΔW gradually decreased from 87.53% to 56.60%, indicating that the wear resistance of the coating gradually
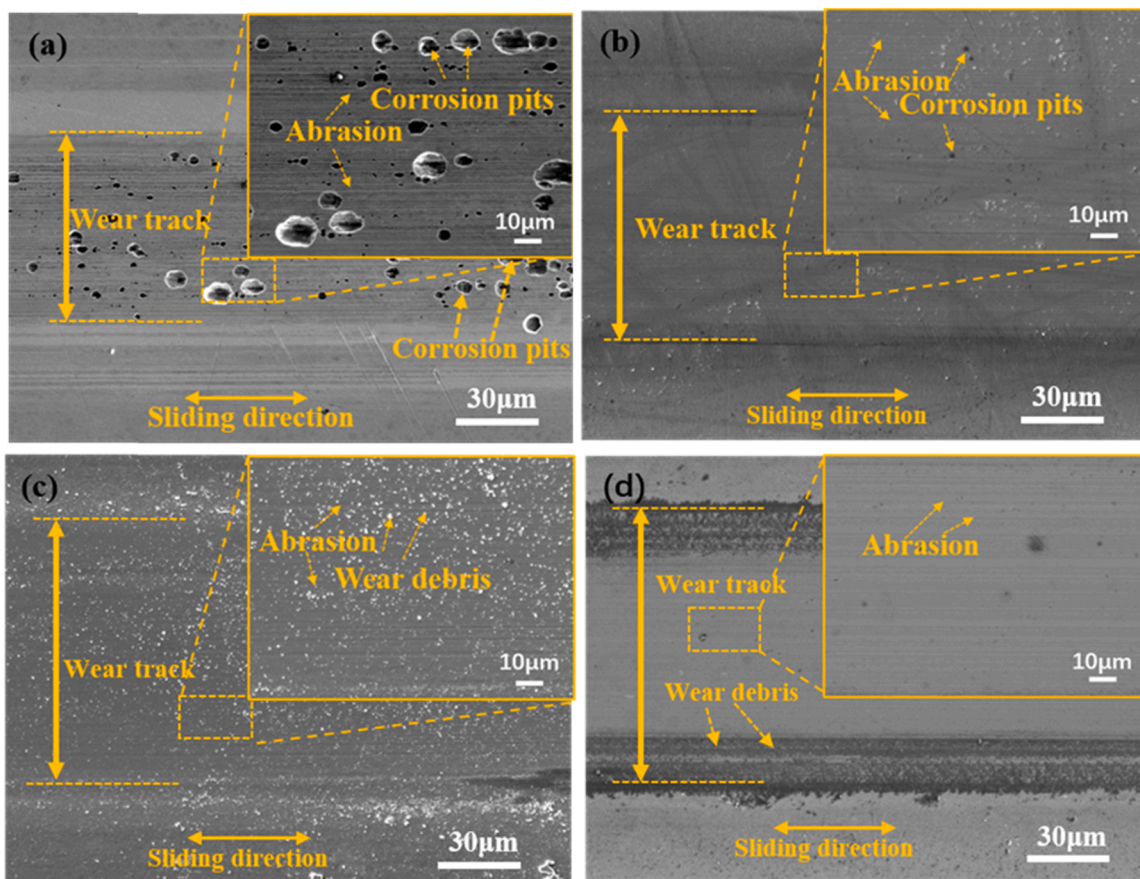
Fig. 9. SEM images of wear track of prepared coatings during tribo-corrosion tests in 3.5 wt% NaCl solution. (a)316 L;(b)S1;(c)S2;(d)S3.

Table 4
Chemical composition of wear tracks during the tribo-corrosion test.

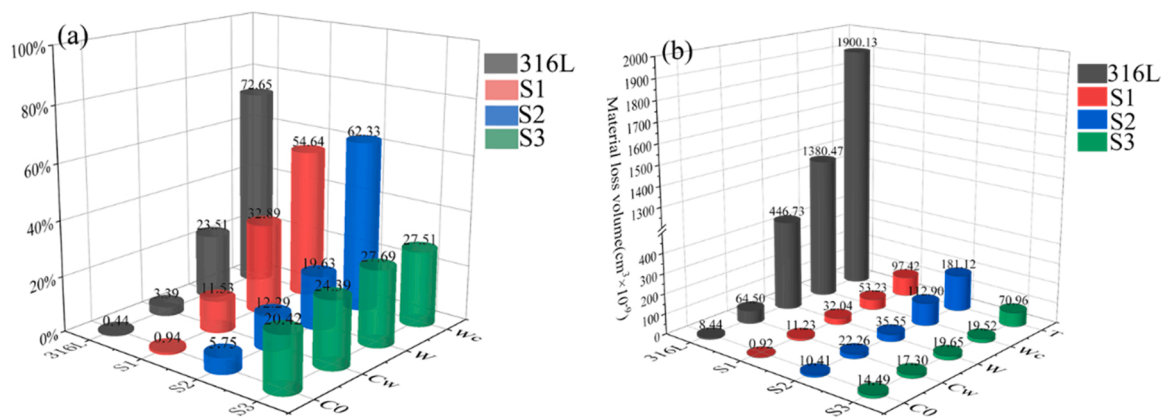| coating	Chemical composition (at%)							
	Ti	Al	Cr	Nb	V	Mo	O	N
S1	2.28399	8.835	8.53399	2.6912	1.94759	4.63881	34.06516	37.004
S2	1.32644	6.141	6.80462	1.5254	1.12747	9.09935	31.87425	42.101
S3	1.69295	4.196	4.71712	1.5772	1.18651	11.9086	16.88612	57.835

Fig. 10. (a) The proportion and (b)volume of each contribution of tribo-corrosion components for 316 L alloy and $(CrNbTiAlVMo)_xN_{1-x}$ coatings sliding against Al_2O_3 balls under polarization condition in 3.5 wt% NaCl solution.

increased with the increase of Mo content. Cr_2O_3 and MoO_3 produced in the friction process can improve the friction of the coating.

Stack et al.[57–59] established the synergism mechanism diagram to explain the synergism in the tribo-corrosion experiment. It can be explained by Fig. 11. By analyzing wear increment (W_C) and total wear volume, the strength of tribo-corrosion synergism between each coating and substrate can be obviously analyzed. It can be seen from Fig. 11 that the synergism of all coatings is weaker than 316 L stainless steel, indicating that corrosion has a great impact on friction. The point of S1 is close to the low synergism region due to its high hardness and Mo make the coating wear-resistant and form more passive MoO_3 film. The hardness of S2 is lower than S1 and the oxide coating of S2 is less than S1. The synergistic effect of S2 is the strongest under the effect of hardness and oxide coating. The dynamic current density of S3 changes little compared to the static current density, the synergy is not obvious, so it falls in the low synergy region.

4. Conclusions

$(CrNbTiAlVMo)_xN_{1-x}$ coating was prepared on 316 L substrate by unbalanced magnetron sputtering. Its microstructure, mechanical properties and tribo-corrosion properties were characterized. The tribo-corrosion synergistic effect of all coatings is stronger than that of 316 L stainless steel. From the experimental results, it can be summarized as follows:

(1) With the increase of Mo content, surface particle size of coating structure is gradually coarse and always maintains a single FCC structure. Mo replaces Cr to form a solid solution. Mixing of multiple elements lowers the free energy and favors the formation of simple solid solutions.

(2) $(CrNbTiAlVMo)_xN_{1-x}$ coatings show good hardness and elasticity when Mo content was 8 at%. With the increase of Mo content, the hardness and elastic modulus of the coating decreased first and then increased.

(3) The tribo-corrosion test results show that the ability to resist synergistic effect of wear and corrosion of all coatings is better than that of 316 L stainless steel in 3.5 wt% NaCl solution. At the 8 at% Mo content, the coatings has the lowest static current density (7.04×10^{-9} A/cm^2) and dynamic current density (9.33×10^{-8} A/cm^2) due to the formation of a large amount of oxide passive film.

(4) The uncoated 316 L steel occurs severe tribo-corrosion in 3.5 wt% NaCl solution, which is significantly affected by the coupling effect of corrosion and wear. The $(CrNbTiAlVMo)_xN_{1-x}$ coated samples exhibit excellent tribo-corrosion performance, and the S3 sample is least affected by the coupling effect of corrosion and wear, which falls in the low synergism region.

Statement of Originality

We declare the following statements:

(1) The article is original.

(2) The article has been written by the stated authors who are ALL aware of its content and approve its submission.

(3) The article has not been published previously.

(4) The article is not under consideration for publication elsewhere.

(5) No conflict of interest exists, or if such conflict exists, the exact nature must be declared.

(6) If accepted, the article will not be published elsewhere in the same form, in English or in any other language, without the written consent of the Publisher.

Declaration of Competing Interest

The authors declare that they have no known competing financial interests or personal relationships that could have appeared to influence the work reported in this paper.

Declaration of competing interest

All the authors declare no competing financial interests for this paper.

Fig. 11. The degree of synergism with *Wc* proportion versus *W* proportion for tribo-corrosion of 316 L and S1, S2, S3 in 3.5 wt% NaCl solution.

References

[1] Robert JK. Wood, Marine wear and tribocorrosion. Wear 2017;376–377:893–910.
[2] Martinelli L, Young DJ, Gossé S, Bosonnet S. Corrosion of 316L in liquid tellurium at 551°C,Corros. Sci 2019;151:35–43.
[3] Monteiro RD, Wetering JVD, Krawczyk B, Engelberg DL. Corrosion behaviour of type 316l stainless steel in hot caustic aqueous environments. Met Mater Int 2020; 26:630–40.
[4] Tan LW, Wang ZW, Ma YL. Tribo-corrosion behavior and degradation mechanism of 316l stainless steel in typical corrosive media. Acta Metall Sin 2021;34:813–24.
[5] Liu HW, Xu DK, Yang K, Liu HF, Cheng YF. Corrosion of antibacterial Cu-bearing 316L stainless steels in the presence of sulfate reducing bacteria. Corros Sci 2018; 132:46–55.
[6] Zou JY, Wang ZW, Ma YL, Tan LW. Tribocorrosion behavior and degradation mechanism of 316L stainless steel in alkaline solution: effect of tribo-film. Acta Metall Sin (Engl Lett) 2022:1–11.
[7] Cook AJMC, Padovani C, Davenport AJ. Effect of nitrate and sulfate on atmospheric corrosion of 304l and 316l stainless steels. J Electrochem Soc 2017; 164:148–63.
[8] Tan LW, Wang ZW, Ma YL. Tribo-corrosion behavior and degradation mechanism of 316l stainless steel in typical corrosive media. Acta Metall Sin (Engl Lett) 2021; 34:813–24.
[9] Nair RB, Arora HS, Mukherjee Sundeep, Singh S, Singh H, Grewal HS. Exceptionally high cavitation erosion and corrosion resistance of a high-entropy alloy. Ultrason Sonochem 2018;41:252–60.
[10] Raza, Abdulahad S, Kang B, Ryu HJ, Hong SH. Corrosion resistance of weight reduced AlxCrFeMoV high-entropy alloys. Appl Surf Sci 2019;485:368–74.
[11] Cui PC, Bao ZJ, Liu Y, Zhou F, Lai ZH, Zhou Y, et al. Corrosion behavior and mechanism of dual phase Fe1.125Ni1.06CrAl high-entropy alloy. Corros Sci 2022; 201:110276..
[12] Yang L, Cheng Z, Zhu WW, Zhao CC, Ren FZ. Significant reduction in friction and wear of a high-entropy alloy via the formation of self-organized nanolayered structure. J Mater Sci Technol 73 2021:1–8.
[13] Xu J, Kong X, Chen MH, Wang QC, Wang FH. High-entropy FeNiCoCr alloys with improved mechanical and tribological properties by tailoring composition and controlling oxidation. J Mater Sci Technol 2021;82:207–13.
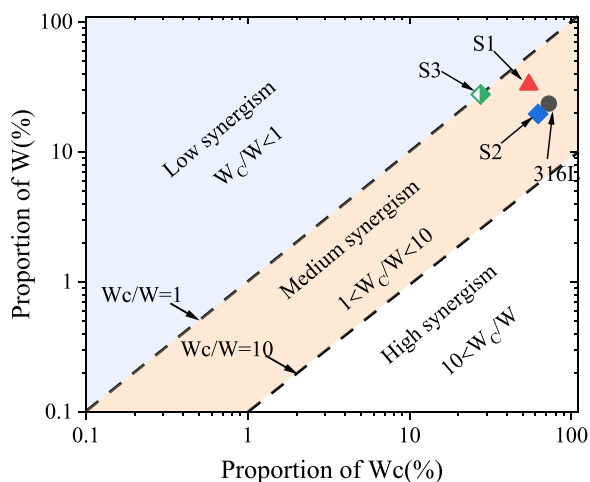
[14] Bhardwaj V, Zhou Q, Zhang F, Han WC, Du Y, Hua K, et al. Effect of Al addition on the microstructure, mechanical and wear properties of TiZrNbHf refractory high-entropy alloys. Tribol Int 2021;160:107031.

[15] Tian YY, Li J, Luo GJ, Fang QH. Tribological property and subsurface damage of nanotwinned Cu/FeCoCrNi high-entropy alloy nanolaminates at various scratching velocities and normal loads. Tribol Int 2022;169:107435.

[16] Xiao Y, Zou Y, Ma H, Sologubenko AS, Maeder X, Spolenak R, et al. Nanostructured NbMoTaW high-entropy alloy thin coatings: high strength and enhanced fracture toughness. Scr Mater 2019;168:51–5.

[17] Zhang ZP, Lei ZF, Huang HL, Liu SF, Zang F, Duan DB, et al. Deformation behavior and toughening of high-entropy alloys. Acta Metal Sin 2018;54:1553–66.

[18] Guo ZM, Zhang AJ, Han JS, Meng JH. Microstructure, mechanical and tribological properties of CoCrFeNiMn high-entropy alloy matrix composites with addition of Cr3C2. Tribol Int 2020;151:106436.

[19] Tsai MH, Yeh JW. High-entropy alloys: a critical review. Mater Res Lett 2014;151: 107–23.

[20] Yeh JW, Chen SK, Lin SJ, Gan JY, Chin TS, Shun TT, et al. Nanostructured high-entropy alloys with multiple principal elements: novel alloy design concepts and outcomes. Adv Eng Mater 2004;6:299–303.

[21] Miracle DB, Senkov ON. A critical review of high-entropy alloys and related concepts. Acta Mater 2017;122:448–511.

[22] Yan XH, Li JS, Zhang WR, Zhang Y. A brief review of high-entropy coatings. Mater Chem Phys 2018;210:12–9.

[23] Li W, Liu P, Liaw PK. Microstructures and properties of high-entropy alloy coatings and coatings: a review. Mater, Res Lett 2018;6:199–229.

[24] Dou D, Li XC, Zheng ZY, Li JC. Coatings of FeAlCoCuNiV high-entropy alloy. Surf Eng 2016;32(10):766–70.

[25] Wang HD, Liu JN, Xing ZG, Ma GZ, Cui XF, Jin G, et al. Microstructure and corrosion behaviour of AlCoFeNiTiZr high-entropy alloy films. Surf Eng 2019;1: 78–85.

[26] Bachani SK, Wang CJ, Lou BS, Chang LC, Lee JW. Microstructural characterization, mechanical property and corrosion behavior of VNbMoTaWAl refractory high-entropy alloy coatings: effect of Al content. Surf Coat Technol 2020;403:126351.

[27] Ren B, Shen ZG, Liu ZX. Structure and mechanical properties of multi-element (AlCrMnMoNiZr)Nx coatings by reactive magnetron sputtering. J Alloy Compd 2013;560:171–6.

[28] Feng XG, Zhang KF, Zheng YG, Zhou H, Wan ZH. Chemical state, structure and mechanical properties of multi-element (CrTaNbMoV)Nx coatings by reactive magnetron sputtering. Mater Chem Phys 2020;239:121991.

[29] Tsai DC, Chang ZC, Kuo BH, Lin TN, Shiao MH, Shieu FS. Interfacial reactions and characterization of (TiVCrZrHf)N thin coatings during thermal treatment. Surf Coat Technol 2014;240:160–6.

[30] Cheng KH, Weng CH, Lai CH, Lin SJ. Study on adhesion and wear resistance of multi-element (AlCrTaTiZr)N coatings. Thin Solid Film 2009;517:4989–93.

[31] Chang SY, Li CE, Chiang SC, Huang YC. 4-nm thick multilayer structure of multi-component (AlCrRuTaTiZr)Nx as robust diffusion barrier for Cu interconnects. J Alloy Compd 2012;515:4–7.

[32] Hsueh HT, Shen WJ, Tsai MH, Yeh JW. Effect of nitrogen content and substrate bias on mechanical and corrosion properties of high-entropy coatings (AlCrSiTiZr)100−xNx. Surf Coat Technol 2012;206:4106–12.

[33] Chang CH, Li PW, Wu QQ, Wang MH, Sung CC, Hsu CY. Nanostructured and mechanical properties of high-entropy alloy nitride coatings prepared by magnetron sputtering at different substrate temperatures. Mater Technol 2019;34: 343–9.

[34] Zhang XY, Pelenovich V, Liu Y, Ke XW, Zhang J, Yang B, et al. Effect of bias voltages on microstructure and properties of (TiVCrNbSiTaBY)N high-entropy alloy nitride coatings deposited by RF magnetron sputtering. Vacuum 2022;195: 110710.

[35] Zhao YM, Chen SJ, Chen YJ, Wu S, Xie WL, Yan WQ, et al. Super-hard and anti-corrosion (AlCrMoSiTi)Nx high entropy nitride coatings by multi-arc cathodic vacuum magnetic filtration deposition. Vacuum 2022;195:110685.

[36] Lo WL, Hsu SY, Lin YC, Tsai SY, Lai YT, Duh JG. Improvement of high entropy alloy nitride coatings (AlCrNbSiTiMo)N on mechanical and high temperature tribological properties by tuning substrate bias. Surf Coat Technol 2020;401: 126247.

[37] Si YX, Wang GG, Wen M, Tong Y, Wang WW, Li Y, et al. Corrosion and friction resistance of TiVCrZrWNx high-entropy ceramics coatings prepared by magnetron sputtering. Ceram Int 2022;48:9342–52.

[38] Ureña J, Tsipas S, Pinto AM, Toptan F, Gordo E, Jiménez-Morales A. Corrosion and tribocorrosion behavior of β-type Ti-Nb and Ti-Mo surfaces designed by diffusion treatments for biomedical applications. Corros Sci 2018;140:51–60.

[39] Yuan XY, Zhao Y, Li X, Chen LQ. Effect of Cr on mechanical properties and corrosion behaviors of Fe-Mn-C-Al-Cr-N TWIP steels. J Mater Sci Technol 2017;33: 1555–60.

[40] Witharamage CS, Christudasjustus J, Smith J, Gao W, Gupta RK. Corrosion behavior of an in situ consolidated nanocrystalline Al-V alloy. NPJ Mater. Degrad 2022;6:1–9.

[41] Fu YQ, Zhou F, Zhang MD. The enhancement of individual friction and corrosion properties of CrSiN coatings by Mo doping in seawater. Surf Coat Technol 2022; 432:128069.

[42] Zou L, Mei FS, Zhang HD, Lin XL, Wang YT, Yuan TC, et al. Improvement of the mechanical, tribological properties and oxidation resistance of AlCrVN coatings by Nb alloying. Ceram Int 2022;48:2555–65.

[43] Jiao Q, Guo FF, Li C, Zheng GF, He JN, Zhao HJ, et al. Effects of Mo addition on tribological performance of plasma–sprayed Ti–Si–C coatings. Ceram Int 2020;46: 12948–54.

[44] Fu YQ, Zhou F, Zhang MD, Wang QZ, Zhou ZF. Structural, mechanical and tribocorrosion performances of CrMoSiN coatings with various Mo contents in artificial seawater. Appl Surf Sci 2020;525:146629.

[45] Lai CH, Lin SJ, Yeh JW, Chang SY. Preparation and characterization of AlCrTaTiZr multi-element nitride coatings. Surf Coat Technol 2006;201:3275–80.

[46] Tsai DC, Chang ZC, Kuo BH, Shiao MH, Chang SY, Shieu FS. Structural morphology and characterization of (AlCrMoTaTi)N coating deposited via magnetron sputtering. Appl Surf Sci 2013;282:789–97.

[47] Tsai DC, Huang YL, Lin SR, Liang SC, Shieu FS. Effect of nitrogen flow ratios on the structure and mechanical properties of (TiVCrZrY)N coatings prepared by reactive magnetron sputtering. Appl Surf Sci 2010;257:1361–7.

[48] Patsalas P, Gravalidis C, Logothetidis S. Surface kinetics and subplantation phenomena affecting the texture, morphology, stress, and growth evolution of titanium nitride films. J Appl Phys 2004;96:6234–46.

[49] Huang PK, Yeh JW. Effects of substrate bias on structure and mechanical properties of (AlCrNbSiTiV)N coatings. J Phys D Appl Phys 2009;42:115401.

[50] Niu YS, Wei J, Yu ZM. Microstructure and tribological behavior of multilayered CrN coating by arc ion plating. Surf Coat Technol 2015;275:332–40.

[51] Zhang MD, Zhou F, Wang QZ, Fu YQ, Zhou ZF. Structural and tribological properties of CrMoCN coatings with various Mo contents in artificial seawater. Appl Surf Sci 2019;493:485–96.

[52] Fu YQ, Zhou F, Zhang MD, Wang QZ, Zhou ZF. Structure and tribocorrosion behavior of CrMoSiCN nanocomposite coating with low C content in artificial seawater. Friction 2021;9:1599–615.

[53] Ma FL, Li JL, Zeng ZX, Gao YM. Structural, mechanical and tribocorrosion behaviour in artificial seawater of CrN/AlN nano-multilayer coatings on F690 steel substrates. Appl Surf Sci 2018;428:404–14.

[54] Lou BY, Wang YX. Effects of Mo content on the microstructure and tribological properties of CrMoAlN films. Acta Metall Sin 2016;52:727–33.

[55] Correa DRN, Kuroda PAB, Grandini CR, Rocha LA, Oliveira FGM, Alves AC, et al. Tribocorrosion behavior of β-type ti-15zr-based alloys. Mater Lett 2016;179: 118–21.

[56] Yan C, Zeng QF, Xu YT, He WJ. Microstructure, phase and tribocorrosion behavior of 60NiTi alloy. Appl Surf Sci 2019;498:143838.

[57] Stack MM, Pungwiwat N. Erosion–corrosion mapping of Fe in aqueous slurries: some views on a new rationale for defining the erosion–corrosion interaction. Wear 2004;256:565–76.

[58] Stack MM, Purandare Y, Hovsepian P. Impact angle effects on the erosion–corrosion of superlattice CrN/NbN PVD coatings. Surf Coat Technol 2004; 188:556–65.

[59] Stack MM, Abd TM. El Badia, Mapping erosion– corrosion of WC/Co–Cr based composite Particle velocity and applied potential effects. Surf Coat Technol 2006; 201:1335–47.